

NH₄CoPO₄·H₂O Microflowers and Porous Co₂P₂O₇ Microflowers: Effective Electrochemical Supercapacitor Behavior in Different Alkaline Electrolytes

Xinjun Wang¹, Zhenzhen Yan^{1,2}, Huan Pang^{*2}, Weiqiang Wang², Guochang Li², Yahui Ma², Hang Zhang², Xuexue Li², Jing Chen^{*2}

¹ College of Chemistry and Chemical Engineering, Henan Normal University, Xinxiang, 455000, Henan, P. R. China.

² College of Chemistry and Chemical Engineering, Anyang Normal University, Anyang, 453000, Henan, P. R. China.

*E-mail: huanpangchem@hotmail.com; chenjing64@eyou.com

Received: 18 December 2012 / Accepted: 12 January 2013 / Published: 1 March 2013

The self-organization of NH₄CoPO₄·H₂O microflowers is successfully synthesized by a mild chemical precipitation method. And different pore sized Co₂P₂O₇ microflowers are synthesized through different calcination temperatures of NH₄CoPO₄·H₂O microflowers. More importantly, supercapacitive performances of NH₄CoPO₄·H₂O microflowers and porous Co₂P₂O₇ microflowers are studied by using cyclic voltammetry (CV), galvanostatic charge/discharge measurements (CP), and electrochemical impedance spectroscopy (EIS) methods in 1.0 M aqueous KOH, NaOH and LiOH solutions. The results show that the crystallinity of materials has largely effect electrochemical activity of supercapacitor in different electrolytes. NH₄CoPO₄·H₂O microflowers exhibit larger supercapacitive characteristics in 1.0 M KOH electrolyte than those of others. The specific capacitance of NH₄CoPO₄·H₂O microflowers electrodes are up to 525 F g⁻¹ at a current density of 0.625 A g⁻¹ and have a long cycle life which have maintained 99.4% after 400 cycles in 1.0 M KOH.

Keywords: Microflower; cyclic voltammetry; galvanostatic charge/discharge; specific capacitance; crystallinity

1. INTRODUCTION

Self-organization is the spontaneous aggregation of molecules into patterns or structures, which is mostly attributed to van der Waals interaction, hydrogen-bonding, electrostatic interaction, etc., where chemistry, biology and materials science overlap [1-4]. In the self-organization, many scientists have successfully controlled nanomaterials by the addition of organic or organometallic molecules as precursors or structure-directing reagents [5, 6]. Patterned-metal-catalyzed routes have also been used

[7-9]. The main drawback of these methods is the need for removal complete template, otherwise impurities will exist in the final products [9-13]. Therefore, there is significant interest in developing spontaneous generation of novel patterns with tailored structures and shapes by facile, hard template-free, solution-based, morphology controlled approaches to building novel self-generated nano/microstructures.

Nowadays, electrochemical supercapacitors, which combine the advantages of both double-layer capacitance and pseudocapacitance, have become a subject of electrochemists. Electroactive materials with several oxidation states or structures, such as transition-metal oxides (e.g., oxides of Ru, Ni, Co, Mn, Mo, Sn, etc.) and conducting polymers are used [14-22]. However, the high cost of Ru has retarded its commercial acceptance as electrode materials in electrochemical capacitors. This limitation has encouraged finding other cheaper materials with similar capacitive behavior to RuO₂. Therefore, it is extremely important to develop alternative electrode material with a combination of low cost and improved performances.

Metal phosphates exhibit broad and potential applications in catalysis [23–26]. A preparation process has been used to synthesize an array of transition-metal phosphate amorphous colloidal spheres by Li et al [23]. Therefore, they have received considerable attention, and some progress has been made [27-30]. Carling and Yuan et al. obtained NH₄M^{II}PO₄·H₂O (M^{II}=Mn, Fe, Co, and Ni) by precipitation from aqueous solution [31-32]. Zhang et al. have successfully reported a general method to prepare metal ammonium phosphate nanoflake constructed microspheres [33]. And Willem K. Kegel et al. have reported the preparation and characterization of colloidal particles of several pyrophosphate metal salts, including, for the first time, salts containing multiple metals [34]. In addition, the transition metal phosphate such as cobalt phosphate can also be act as the promising positive electrodes for rechargeable ion batteries, heterogeneous catalysts, sorbents, ion exchangers, and magnetism materials due to the layers of connected CoO_x and PO₄ polyhedra, the structures of known zeolite types, and the outstanding electronic or magnetic property [35-40]. However, there are little reports about the electrochemical capacitor properties of cobalt phosphate material [41].

In this work, we have successfully synthesized cobalt ammonium phosphate with microflowers by a very simple and mild chemical precipitation method without templates or surfactants. Furthermore, different pore sized cobalt pyrophosphate microflower materials have also been obtained by different thermal decompositions of the as-synthesized NH₄CoPO₄·H₂O microflowers in the air. The electrochemical properties of NH₄CoPO₄·H₂O microflowers and porous Co₂P₂O₇ materials are studied systematically for their applications as electrochemical capacitor electrode materials in different alkaline electrolytes. We find that the crystallinity of materials has largely effect electrochemical activity of supercapacitor. Among these materials, NH₄CoPO₄·H₂O microflowers exhibit larger supercapacitive characteristics in 1.0 M KOH electrolyte than others. The specific capacitance of NH₄CoPO₄·H₂O microflowers electrodes are up to 525 F g⁻¹ at current density of 0.625 A g⁻¹ and have a long cycle life which have maintained 99.4% after 400 cycles in 1.0 M KOH electrolyte.

2. EXPERIMENTAL

2.1 Self-organization synthesis of $\text{NH}_4\text{CoPO}_4\cdot\text{H}_2\text{O}$ microflowers

In a typical synthesis, 3.0 g of ammonium phosphate were added to a beaker within 20 mL deionized water and 20 mL polyethylene glycol 600 (PEG 600), the above mixture was stirred at room temperature until solid completely dissolved. Then, 0.2 g cobalt chloride was added into the mixed solution with vigorous magnetic stirring at room temperature for 4 h. The obtained homogeneous purple precipitates were washed several times by deionized water, ethanol, and dried at 50 °C in the air. The product was named M.

The conversion of $\text{NH}_4\text{CoPO}_4\cdot\text{H}_2\text{O}$ to $\text{Co}_2\text{P}_2\text{O}_7$ was carried out in a muffle in air at a heating rate of 1 °C/min: 480 °C for 10 min, the product was named P1; 550 °C for 10 min, the product was named P2; 600 °C for 10 min, the product was named P3.

2.2 Electrochemical measurement

Electrochemical study on $\text{NH}_4\text{CoPO}_4\cdot\text{H}_2\text{O}$ and $\text{Co}_2\text{P}_2\text{O}_7$ electrodes were carried out on a CHI 660D electrochemical working station (ChenHua Instrument, Inc.). All electrochemical performances were carried out in a conventional three-electrode system equipped with platinum electrode and a saturated calomel electrode (SCE) as counter and reference electrodes, respectively. Before electrochemical measurement, we have purged out O_2 from the solution by the inert gas-Ar. The working electrode was made from mixing of active materials ($\text{NH}_4\text{CoPO}_4\cdot\text{H}_2\text{O}$ or $\text{Co}_2\text{P}_2\text{O}_7$), acetylene black, and PTFE (polytetrafluoroethylene) with a weight ratio of 85:15:5, coating on a piece of foamed nickel of about 1 cm², and pressing to be a thin foil at a pressure of 5.0 MPa. The electrolyte was 1.0 M KOH, NaOH, or LiOH solution. Cyclic voltammetry and galvanostatic charge–discharge methods were used to investigate capacitive properties of $\text{NH}_4\text{CoPO}_4\cdot\text{H}_2\text{O}$ or $\text{Co}_2\text{P}_2\text{O}_7$ electrodes. And electrochemical impedance spectroscopy measurements of all the samples were conducted at open circuit voltage in the frequency range of 100 kHz to 0.01 Hz with AC voltage amplitude of 5 mV using PARSTAT2273.

2.3. Sample characterization

The morphology of as-prepared samples was observed by a JEOL JSM-6701F field-emission scanning electron microscope (FE-SEM) at an acceleration voltage of 5.0 kV. The phase analyses of the samples were performed by X-ray diffraction (XRD) on a Rigaku-Ultima III with Cu K_α radiation ($\lambda = 1.5418 \text{ \AA}$). Thermo-gravimetric analysis (TG) was carried out in air up to 800 °C using a NETZSCH STA 409 PC instrument with a heating rate of 5 °C/min. Nitrogen adsorption-desorption measurements were performed on a Gemini VII 2390 Analyzer at 77 K using the volumetric method. The specific surface area was obtained from the N_2 adsorption-desorption isotherms and was calculated by the Brunauer-Emmett-Teller (BET) method. Transmission electron microscopy (TEM)

images and HRTEM image were captured on the JEM-2100 instrument microscopy at an acceleration voltage of 200 kV.

3. RESULTS AND DISCUSSION

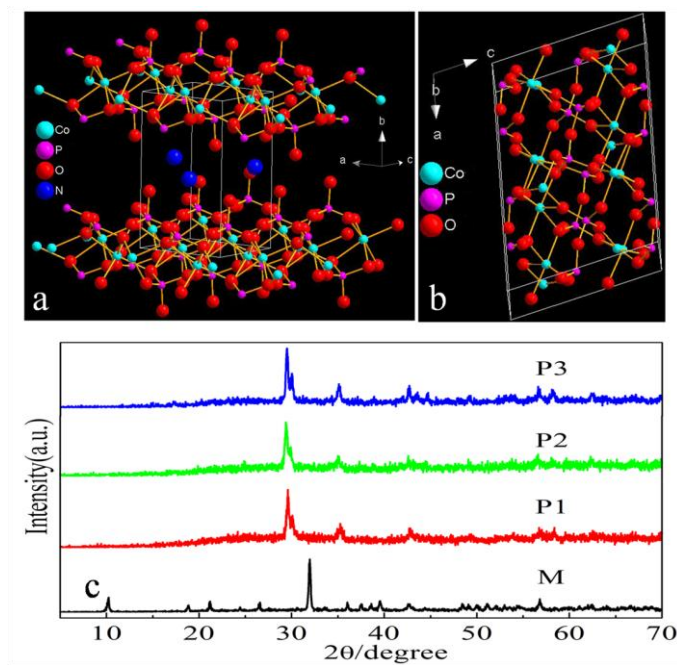


Figure 1. Schematic crystal structures of unit cell: (a) $\text{NH}_4\text{CoPO}_4 \cdot \text{H}_2\text{O}$; (b) $\text{Co}_2\text{P}_2\text{O}_7$; (c) XRD patterns of $\text{NH}_4\text{CoPO}_4 \cdot \text{H}_2\text{O}$ (M) and porous $\text{Co}_2\text{P}_2\text{O}_7$ microflowers (P1, P2 and P3).

Fig. 1 (a, b) shows schematic crystal structures of unit cell of $\text{NH}_4\text{CoPO}_4 \cdot \text{H}_2\text{O}$ and $\text{Co}_2\text{P}_2\text{O}_7$. In Fig. 1a, it is clear that $\text{NH}_4\text{CoPO}_4 \cdot \text{H}_2\text{O}$ has a layer crystal structure and there are many nanogaps between layer crystal structures which might make ion or electrolyte access easily along these gaps, while that of $\text{Co}_2\text{P}_2\text{O}_7$ crystal structure do not has in Fig. 1b. Fig. 1c shows XRD patterns of samples (M) and samples (P1-P3). Powder XRD characterizations confirm that $\text{NH}_4\text{CoPO}_4 \cdot \text{H}_2\text{O}$ nanocrystallites have been obtained under our experimental conditions with high purity and good crystallinity in Fig. 1c, which can be indexed to be in agreement with $\text{NH}_4\text{CoPO}_4 \cdot \text{H}_2\text{O}$ (JCPDS NO. 21-0793). Such good crystallinity of M is good for improving cycle life of electrodes for its stable structure which is not easily to destroy during the electrochemical process.

The size and shape of as-prepared $\text{NH}_4\text{CoPO}_4 \cdot \text{H}_2\text{O}$ were examined by field emission scanning electron microscopy (FE-SEM). Fig. 2a shows FE-SEM images of $\text{NH}_4\text{CoPO}_4 \cdot \text{H}_2\text{O}$ samples obtained within 17-18 μm . It indicates that the sample almost completely consists of many plate structures in Fig. 2b. From images of Fig. 2c, we can see that nanoplates have assembled as a flower structure. When assembling, there are many nanogaps formed within 8-10 nm in Fig. 2d. These nanogaps might have many channels to let ions go through, which might enhance the travelling speed of ions and thus bring the high specific capacitances.

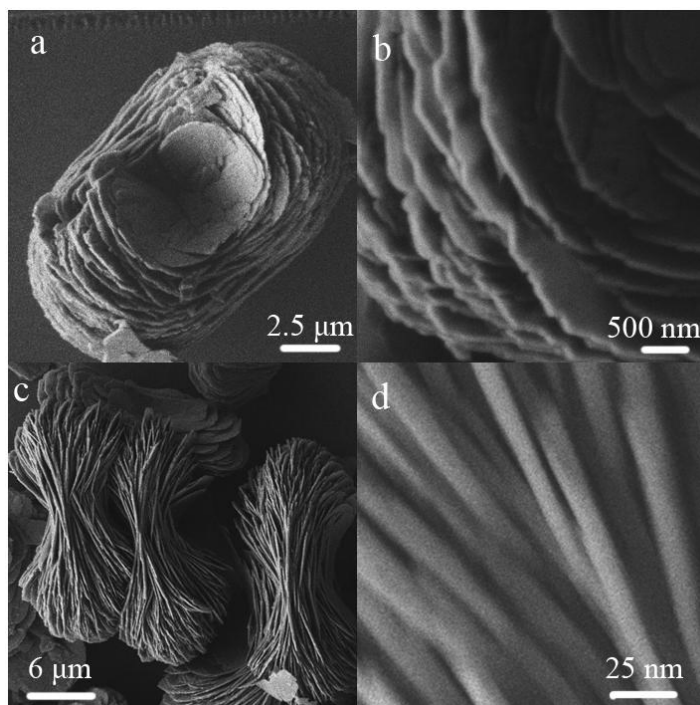


Figure 2. (a-d) SEM images of $\text{NH}_4\text{CoPO}_4 \cdot \text{H}_2\text{O}$ microflowers (M).

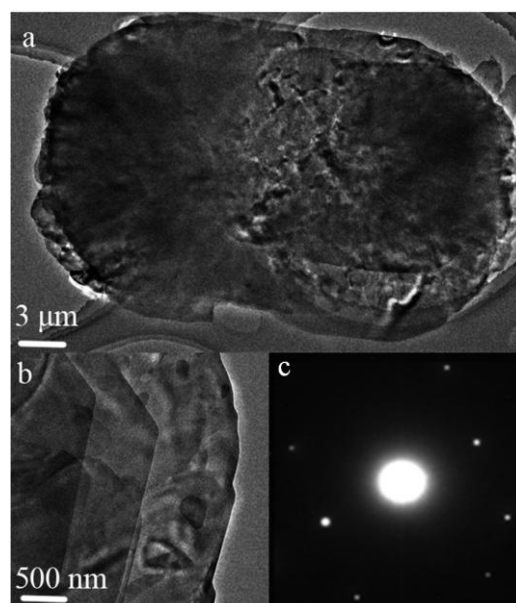


Figure 3. (a, b) TEM images of $\text{NH}_4\text{CoPO}_4 \cdot \text{H}_2\text{O}$ microflowers (M); (c) Selected area diffraction (SAED) patterns of M.

Fig. 3 (a, b) displays TEM images of $\text{NH}_4\text{CoPO}_4 \cdot \text{H}_2\text{O}$ microflowers. In Fig. 3 (a, b), several plates overlap and assemble together, and then form $\text{NH}_4\text{CoPO}_4 \cdot \text{H}_2\text{O}$ microflowers. The surface of unit plate is very smooth, and from SAED image of Fig. 3c, the unit-plate is a single crystal structure,

whose good crystallinity might offer a stable structure for diffusion of ions or electrolytes to improve cycle life of electrodes.

Porous $\text{Co}_2\text{P}_2\text{O}_7$ microflowers were obtained easily by calcining $\text{NH}_4\text{CoPO}_4\cdot\text{H}_2\text{O}$ in the air. Electronic Supplementary Information (ESI) Fig. 1 shows TG curve of $\text{NH}_4\text{CoPO}_4\cdot\text{H}_2\text{O}$ microflowers from ambient temperature to 800 °C. The TG curve shows that thermal decomposition of $\text{NH}_4\text{CoPO}_4\cdot\text{H}_2\text{O}$ microflowers below 800 °C occurs in two weight loss steps. Fig. 1b-d shows XRD patterns of all the $\text{Co}_2\text{P}_2\text{O}_7$ samples (P1-P3). All of the reflection peaks in XRD patterns match well with the standard pattern of $\text{Co}_2\text{P}_2\text{O}_7$ (JCSPDF card No: 49-0191). Powder XRD characterizations confirm that $\text{Co}_2\text{P}_2\text{O}_7$ micro-nanostructures have successfully obtained under our experimental conditions with good purity and crystallinity. And P3 has the best crystallinity in the $\text{Co}_2\text{P}_2\text{O}_7$ micro-nanostructures for long time heated temperature.

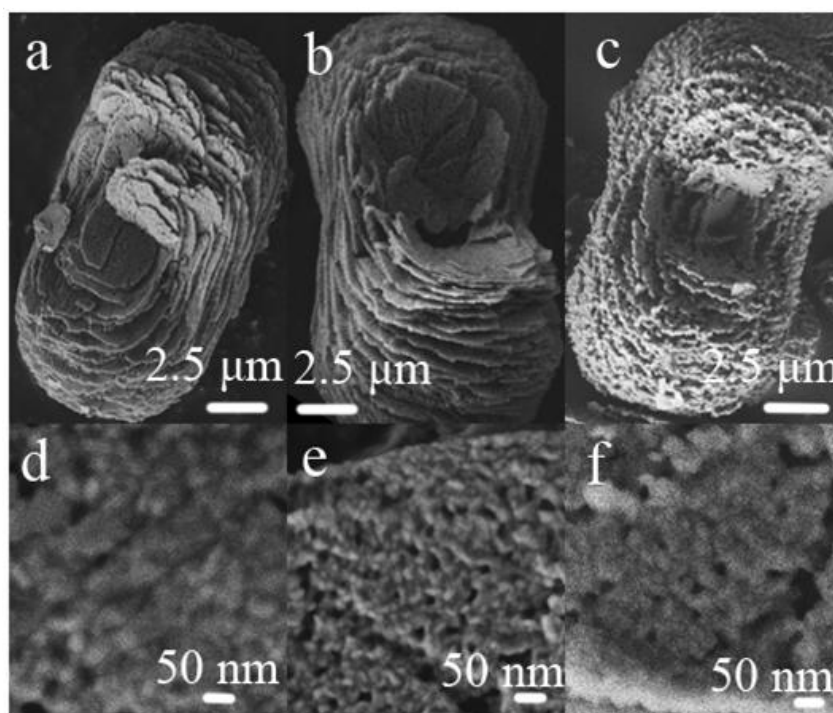


Figure 4. SEM images of $\text{Co}_2\text{P}_2\text{O}_7$ samples: (a, d) P1; (b, e) P2; (c, f) P3.

Fig. 4 displays FE-SEM images of $\text{Co}_2\text{P}_2\text{O}_7$ samples (P1-P3). A low magnification FE-SEM image of P1-P3 is shown in Fig. 4a-c. It shows that the product has maintained the morphology of M, and shows porous structures of P1-P3. Unlike M1, P1-P3 both have partly maintained nanogaps and generated many new nanopores which might cause by decomposition of M1 and the released gases. During the calcination process from $\text{NH}_4\text{CoPO}_4\cdot\text{H}_2\text{O}$ to $\text{Co}_2\text{P}_2\text{O}_7$, the loss of water and ammonia would cause the shrinkage and a different shrinkage velocity at different parts of materials would lead to the formation of pores. Porous microflowers of P1-P3 are assembled by several porous nanoplates which form many nanogaps. There are also some differences in Fig. 4, such as the intensity of rough surface is $\text{P1} < \text{P2} < \text{P3}$. And the porous microflower structure might offer a stable structure for ion

intercalated/extracted into/out and electrolyte access, which might improve the cycle life of the electrode [42–46].

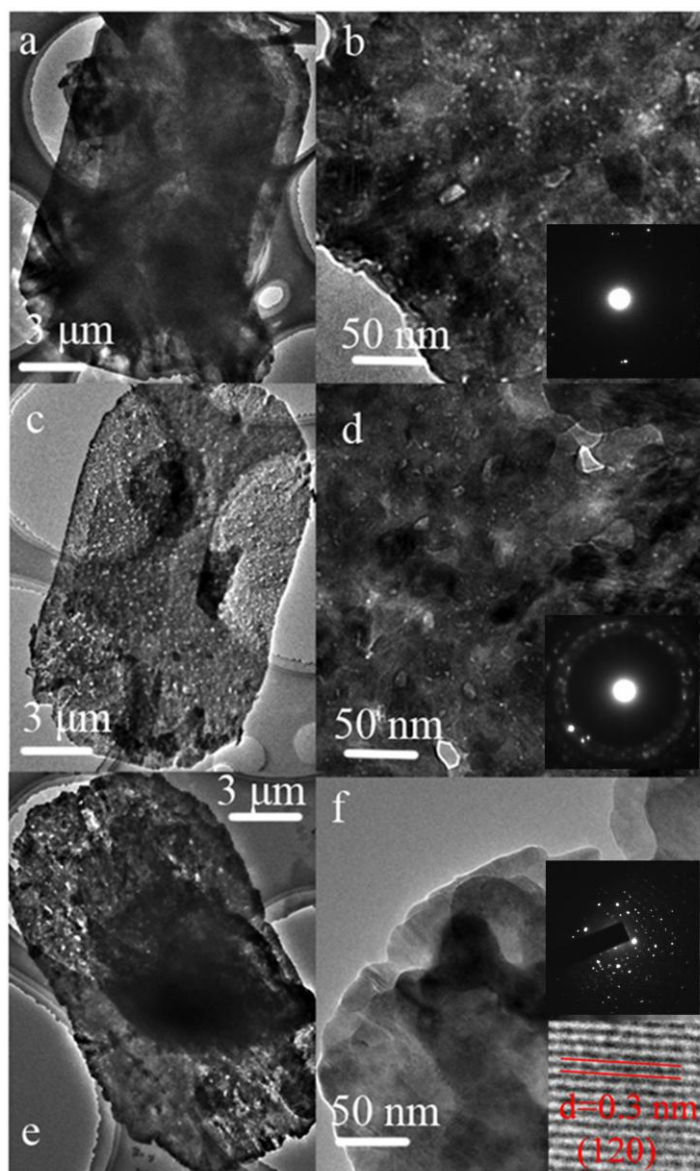


Figure 5. TEM images of $\text{Co}_2\text{P}_2\text{O}_7$ samples: (a, b) P1; (c, d) P2; (e, f) P3; In inset of b, d, f, SAED patterns of samples.

To more clearly and correctly describe porous properties of P1-P3 materials, TEM images of all samples were shown in Fig. 5. All the samples show the porous structure, especially for pores of P1 are distributed homogeneously among the small primary particles (several nanometers) throughout the whole microflower structures (several micrometers). There are thousands of pores in a microflower structure for P1. HRTEM results of P1 have been shown in Fig. 5b. And we found that there are many pores for P1 with size ≤ 5 nm in Fig. 5b. Small size pores of P2 have partly disappeared due to the growth of building block particle in Fig. 5d. When heated under 600 °C for 10 min to obtain P3, the

building block particle has fused together and tried to form the single crystal in Fig. 5f. The selected area diffraction (SAED) patterns of samples are shown in inset of Fig. 5b, d, f. It is clear that P3 has the best crystalline which is proved by its punctate SAED patterns. What is more, an inter-planar spacing of 0.30 nm of P3 is corresponding to the separation between the (120) lattice planes of $\text{Co}_2\text{P}_2\text{O}_7$ JCPDS-49-0191 in inset of Fig. 5f.

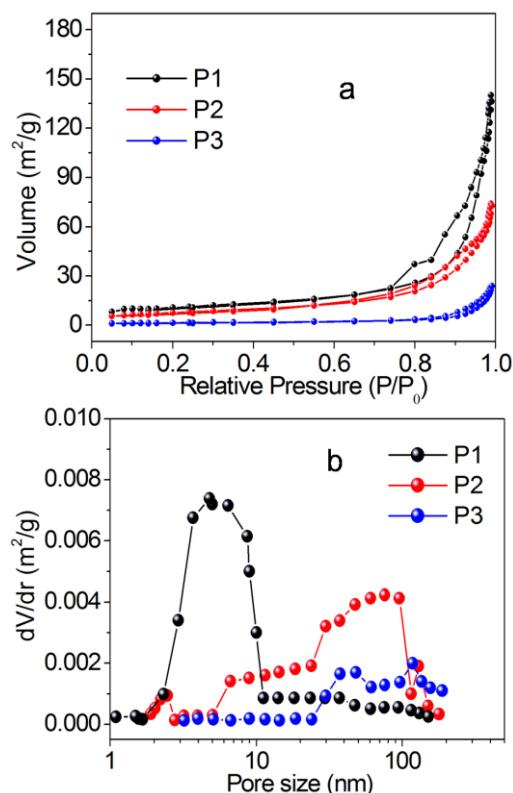


Figure 6. (a) Brunauer–Emmett–Teller measurements of samples; (b) Corresponding Barrett–Joyner–Halenda pore size distribution curves.

To gain further insight into the porous structure and size distribution of samples, Brunauer–Emmett–Teller (BET) measurements were performed to examine their specific structural properties. The products of P1 and P2 show a distinct hysteresis in the larger range ca. 0.75–1.0 P/P_0 in Fig. 6a, indicating the presence of mesopores possibly formed by porous stacking of component nanoparticles. The BET surface area of P1 ($33.1 \text{ m}^2\text{g}^{-1}$) is much larger than that of P2 ($13.6 \text{ m}^2\text{g}^{-1}$) and P3 ($9.1 \text{ m}^2\text{g}^{-1}$) making an efficient contact of activated materials with electrolyte. The corresponding Barrett–Joyner–Halenda (BJH) pore size distribution curves (Fig. 6b) show that the pore size of P1 is uniform, within the range of the mesopores (2–10 nm), while those of P2 and P3 are not such uniform, within the range of pores (10–100 nm). The porous structures of P1 could offer high surface areas which make an efficient contact of P1 with electrolyte.

Specific capacitances derived from cyclic voltammetry (CV) tests can be calculated from the following equation [47]:

$$C = \frac{1}{m\nu(V_c - V_a)} \int_{V_a}^{V_c} I(V)dV \quad (1)$$

where C ($F g^{-1}$), m (g), ν ($V s^{-1}$), V_c and V_a , and I (A) are the specific capacitance, the mass of the active materials in the electrode, potential scan rate, high and low potential limit of the CV tests, and the instant current on CV curves, respectively.

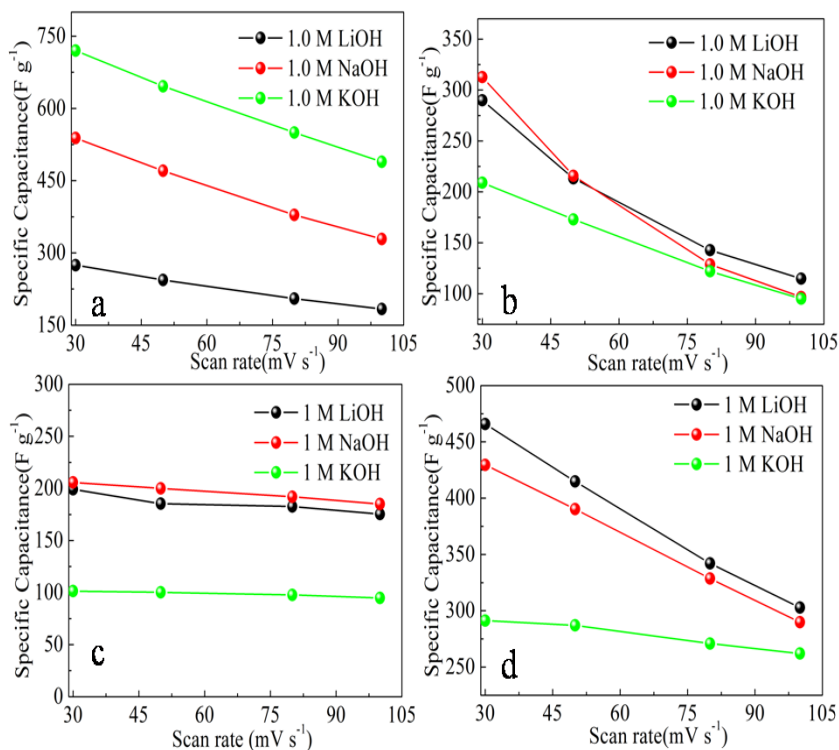


Figure 7. Specific capacitances of electrode materials at different scan rates derived from cyclic voltammetry in 1.0 M LiOH, NaOH and KOH aqueous solutions: (a) M; (b) P1; (c) P2; (d) P3.

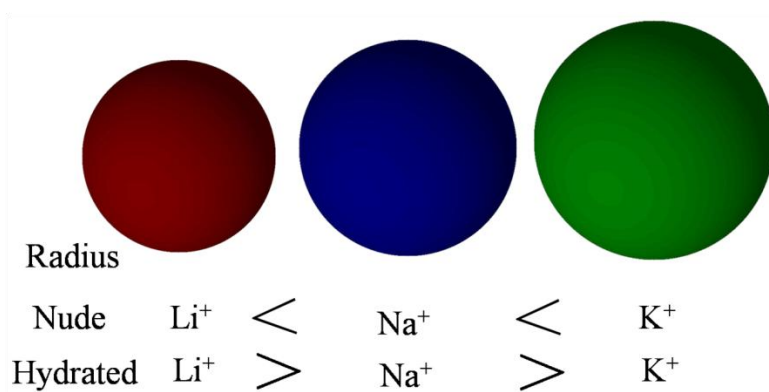


Figure 8. Ions radius in aqueous solutions.

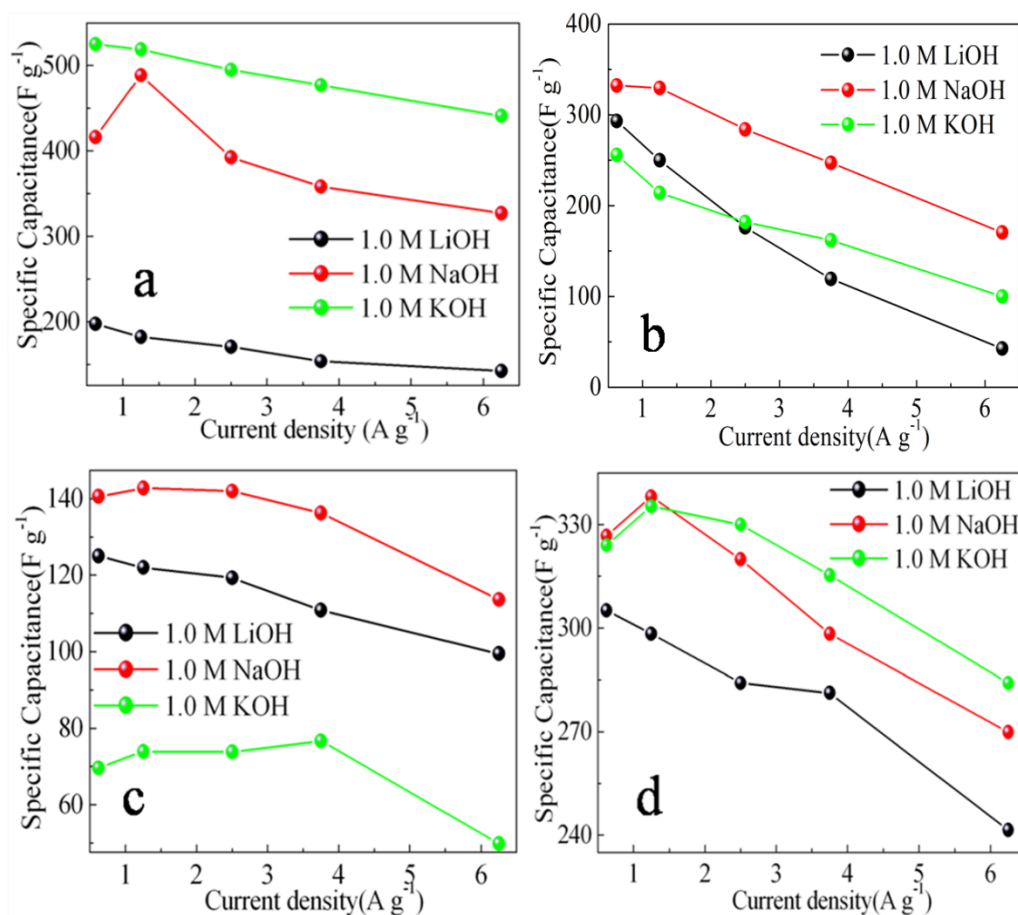


Figure 9. Specific capacitances of electrode materials at different current densities derived from galvanostatic charge–discharge curves in 1.0 M LiOH, NaOH and KOH aqueous solutions: (a) M; (b) P1; (c) P2; (d) P3.

The specific capacitances calculated from CV curves at scan rates of 30–100 mV s⁻¹ in 1.0 M aqueous LiOH, NaOH and KOH solutions are respectively shown in Fig. 7. From Fig. 7a, the specific capacitance of M can achieve 720 F g⁻¹ in 1.0 M KOH at 30 mV s⁻¹. It is larger than those of M in other electrolytes, which might cause by different hydrated ion radius. It is important that hydrate ion radius is $(r_{\text{Li}^+(\text{H}_2\text{O})}) > r_{\text{Na}^+(\text{H}_2\text{O})} > r_{\text{K}^+(\text{H}_2\text{O})}$ in Fig. 8 [48]. And different hydrated ions always have different intercalated/extracted into/out rates for layer crystal structures of $\text{NH}_4\text{CoPO}_4 \cdot \text{H}_2\text{O}$ (M) microflowers.

It is clear that specific capacitance of porous $\text{Co}_2\text{P}_2\text{O}_7$ microflowers at the lowest scan rate is the largest one in different electrolytes. Observing from all the curves in Fig. 7, we find that the specific capacitance has decreased as the increasing of scan rate. More interesting, the electrochemical supercapacitor properties of porous $\text{Co}_2\text{P}_2\text{O}_7$ microflowers in 1.0 M aqueous LiOH and NaOH solutions are more effective than those of in KOH solution. This result is not according with the conclusion of Fig. 7a, and the electrochemical capacitor activity of $\text{Co}_2\text{P}_2\text{O}_7$ might be reduced by the polarity of alkaline electrolytes due to the stable of $\text{P}_2\text{O}_7^{4-}$ group ($2\text{OH}^- + \text{P}_2\text{O}_7^{4-} \rightleftharpoons 2\text{PO}_4^{3-} + \text{H}_2\text{O}$). The good crystallinity of P3 might reduce this possible reaction for the stable structure, while the defect structure of P1 and P2 makes the possible reaction happen.

The specific capacitance of an electrode during galvanostatic charge/discharge can be calculated by the following equation [47]:

$$C = \frac{i \cdot \Delta t}{m \cdot \Delta V} \quad (2)$$

Where m is the mass of $\text{NH}_4\text{CoPO}_4 \cdot \text{H}_2\text{O}$ or $\text{Co}_2\text{P}_2\text{O}_7$ (g), ΔV is the range of charge/discharge (V), and i is the discharge current (A) applied for time Δt (s).

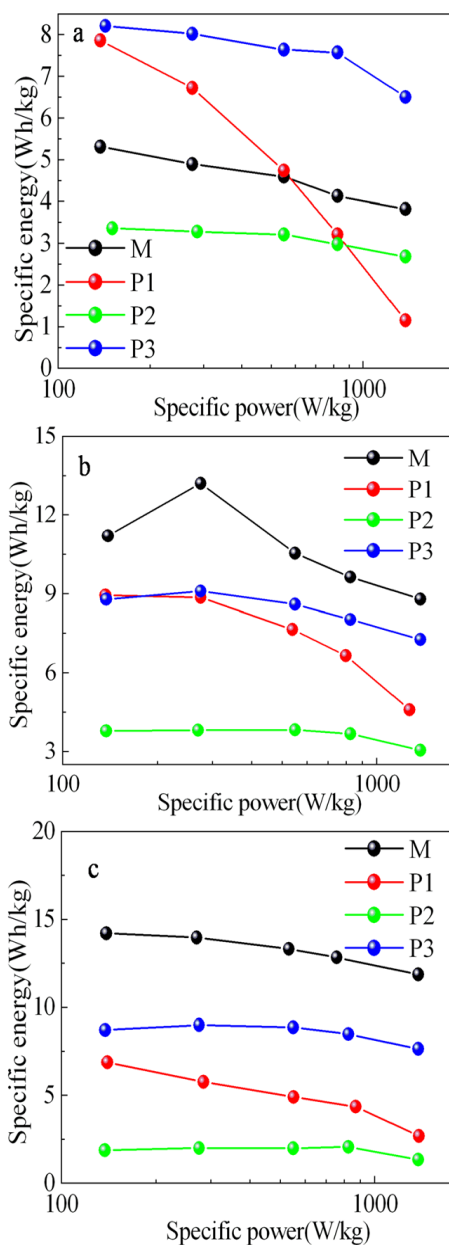


Figure 10. Ragone plot of the estimated specific energy and specific power at various current densities in 1.0 M aqueous solutions: (a) LiOH; (b) NaOH; (c) KOH.

The specific capacitances derived from the discharging curves at the current density of 0.625-6.25 A g⁻¹ are shown in Fig. 9. In Fig. 9a, M also has the largest specific capacitance than those of other electrodes in 1.0 mol L⁻¹ KOH. The specific capacitance of M at the current density of 0.625 A g⁻¹ is calculated to be 525 F g⁻¹ in 1.0 M KOH solution. As the increasing current density to 6.25 A g⁻¹, the specific capacitance of M also have 441 F g⁻¹ in 1.0 M KOH solution. Compared with KOH solution, the electrochemical activity of M in LiOH solution has also been limited due to hydrate ion radius. From Fig. 9b-d, P3 has much stable specific capacitance (0.625 A g⁻¹-327 F g⁻¹; 6.25 A g⁻¹-270 F g⁻¹) in KOH solution, which might cause by its crystallization, because P3 was obtained under 600 °C for 10 min which has good crystallization. There might be little change for a stable crystal structure during the ion intercalated/extracted into/out, and SEM images of M and P1-P3 after 400 cycle tests are shown in ESI Fig. 2. It is clear that M and P3 have partly maintained the microstructure as before 400 cycle tests. M has partly fused and become a large microflower, while P1 and P2 have transformed to random slices.

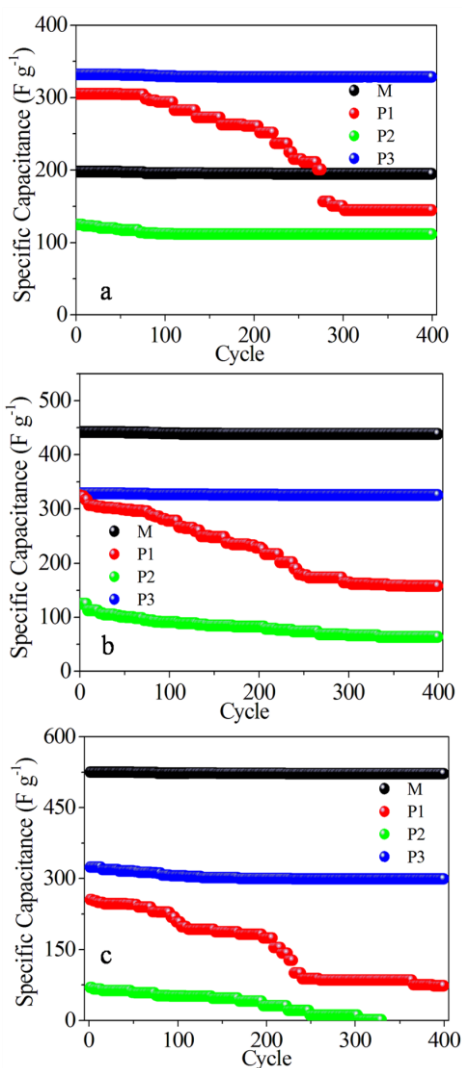


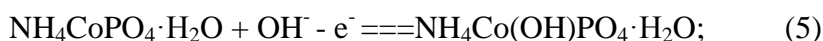
Figure 11. Charge/discharge cycling tests at current density of 0.625 A g⁻¹, 1.0 M aqueous solutions: (a) LiOH; (b) NaOH; (c) KOH.

Besides large specific capacitance, another advantage of supercapacitors is that they have both large power density and energy density. This unique property ensures the wide application of supercapacitors in many practical fields. Fig. 10 shows the Ragone plot for four electrodes in different aqueous solutions. In Fig. 10a, P3 has larger energy density and powder density than those of others in LiOH solution, whose the specific energy decreases from 8.2 to 6.5 Wh kg⁻¹, while the specific power of P3 increases from 142.8 to 1376 W kg⁻¹ as the GV charge/discharge current increasing from 0.625 to 6.25 A g⁻¹. The specific energy of P1 decreases largely from 7.86 to 1.15 Wh kg⁻¹ in LiOH solution.

In Fig. 10 (b, c), M has both large power density and energy density, other sequence is P3, P1, P2. In Fig. 10c, the specific energy of M decreases from 14.2 to 11.9 Wh kg⁻¹, while the specific power increases from 139 to 1377 W kg⁻¹ as the GV charge/discharge current increases from 0.625 to 6.25 A g⁻¹ in KOH solution. For comparison, in Fig. 10c, the smallest specific energy of P2 decreases from 2.0 to 1.34 Wh kg⁻¹, while the specific power increases from 275.0 to 1375 W kg⁻¹ as the GV charge/discharge current increases from 0.625 to 6.25 A g⁻¹ in KOH solution.

It is also very important for electrode materials to have good specific capacitance retention. The supercapacitors should work steadily and safely, which requires the specific capacitance of electrode materials to change as little as possible. The morphology of electrode materials might offer different stable structures for ion intercalated/extracted into/out, which might bright different cycle life of electrodes [49-53]. The relationship of cycling number and specific capacitance in different solutions are shown in Fig. 11. It is obvious that P3 and M electrodes have good cycle life in 1.0 M LiOH solution in Fig. 11a. More importantly, it also shows excellent specific capacitance retention of M in 1.0 M NaOH or KOH solution in Fig. 11 b, c. After 100 continuous charge–discharge cycles, M almost has the same specific capacitance as its initial value, while others drop. Even after 400 continuous charge–discharge cycles, the specific capacitance of M have retained more than 99.4 % and is about 522 F g⁻¹, which is still quite a large value in Fig. 11c. We consider that different cycle life of electrodes might caused by different crystallinity of samples. Though P1 has large BET surface area than other, the poor crystallinity might make its cycle life limited. M and P3 have better crystallinity than those of others, which result in good cycle life. The little drop of specific capacitance of M possibly results from the slight collapse of the novel microflower, when ions intercalate and extract into the novel microflower in ESI Fig. 2a, while others have become randomly slices.

We have proposed the possible mechanism-eq. 5, 6 to explain the intercalated/ extracted of ions in NH₄CoPO₄·H₂O and Co₂P₂O₇ nano/micromaterials.



To identify the exact electrical conductivity of electrodes, we measured EIS spectrum of NH₄CoPO₄·H₂O, Co₂P₂O₇ nano/microstructures at room temperature in the frequency range 0.01–10⁵ Hz under open-circuit conditions, which are shown in Fig. 12a-c. In general, the impedance curves present two partially overlapped semicircles in the high and medium frequency regions and an inclined line in the low-frequency region. An equivalent circuit used to fit the impedance curve is given in Fig.

12d, which is similar to the circuit employed for the working electrode of supercapacitor. The EIS data can be fitted by a bulk solution resistance R_s , a charge-transfer R_{ct} and a pseudocapacitive element C_p from redox process of electrode materials, and a CPE to account for the double-layer capacitance.

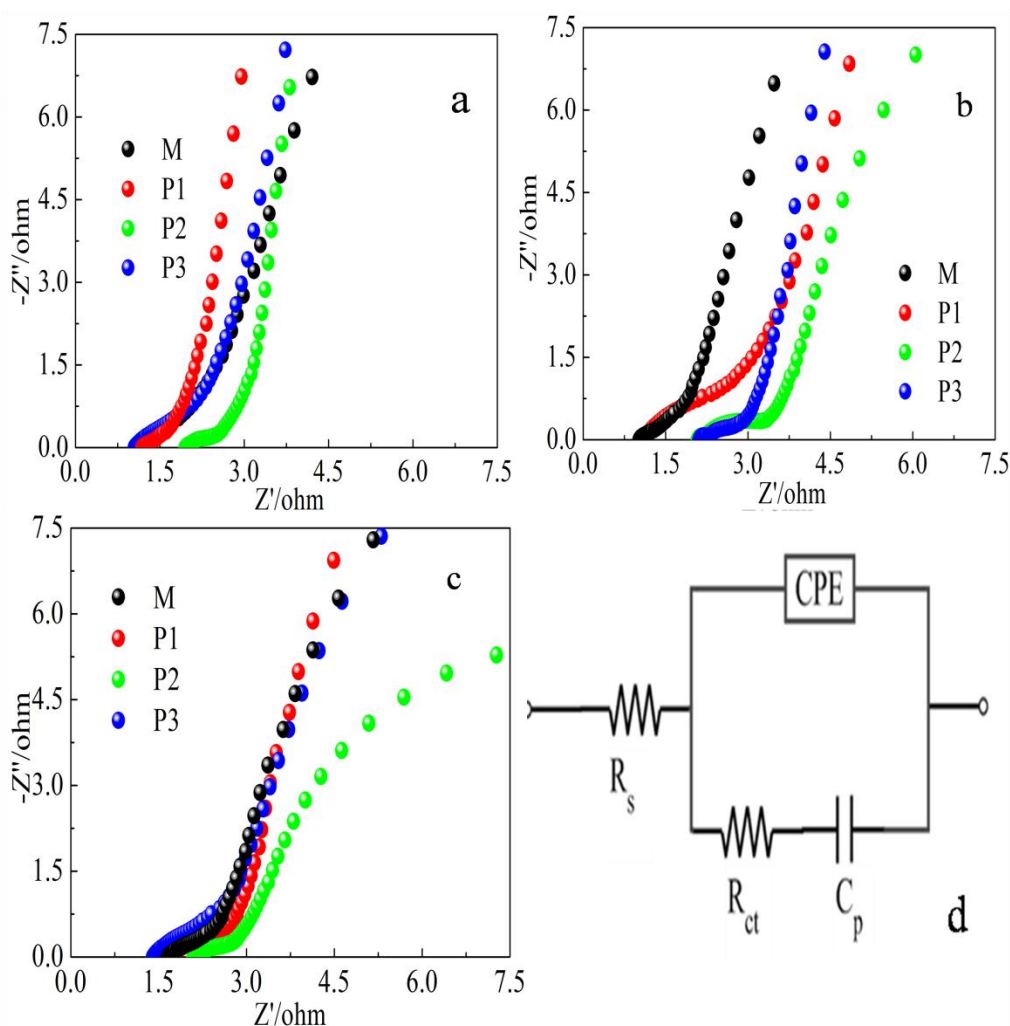


Figure 12. Electrochemical impedance spectra (EIS) for M, P1-P3 electrodes under room temperature in 1.0 M aqueous solutions: (a) LiOH; (b) NaOH; (c) KOH; (d) An equivalent circuit consisting of a bulk solution resistance R_s , a charge-transfer R_{ct} , a pseudocapacitive element C_p from redox process of electrodes, and a constant phase element (CPE) to account for the double-layer capacitance.

The charge-transfer resistance R_{ct} of all the sample was calculated (ZSimpWin software). And from the calculated results, we find that M has both lower value-4.1 Ω in KOH solution and 5.5 Ω in NaOH solution, and P3 has lowest value-8.6 Ω in LiOH solution. And detailed R_{ct} values of others in LiOH, NaOH and KOH solutions are shown in ESI Table 1. This clearly demonstrates the charge-transfer resistance of electrodes is connected with electrode materials, morphologies and electrolytes. In addition, the charge-transfer resistance R_{ct} , also called Faraday resistance, is a limiting factor for the

specific power of the supercapacitor. It is the low Faraday resistance that results in the high specific power of the M electrode in KOH solution.

Such superior rate capability of the electrode might be attributed to many reasons. The reason which causes to change diffusion paths of ions or electrolytes is the key one. Such as: (1) highly accessible surface area for nanopores or nanochannels; (2) good conductivity of materials; (3) different crystallinity of materials and so on. From BET measurements of samples, we also found that BET surface area of M ($10.2 \text{ m}^2 \text{ g}^{-1}$) and P3 ($9.1 \text{ m}^2 \text{ g}^{-1}$) is not very large, but M and P3 has better electrochemical activities than others in different electrolytes. We could conclude that the conductivity of electrode plays a key pole in this work, and from Ragone plot in Fig. 12, it is integrated results of electrochemical supercapacitor. Different surface-interface characters and conductivities might have different chemical-physical adsorption-desorption abilities towards the ion and diffusion path of ions, resulting in different electrochemical activities.

4. CONCLUSIONS

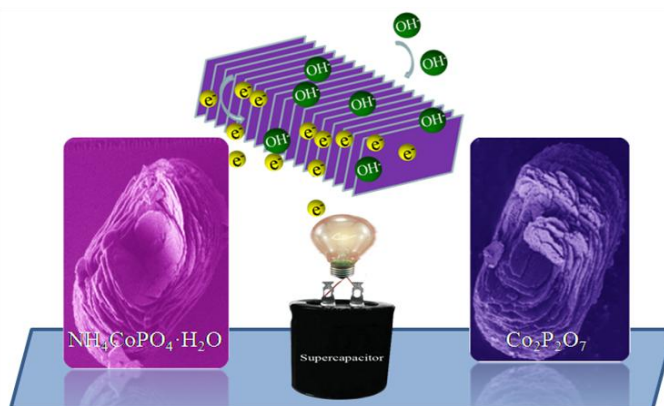


Figure 13. A simple scheme of growth and synthesis of materials, and possible charge-discharge processing.

This work can be simple decript as Fig. 13. In this work, we successfully synthesized cobalt ammonium phosphate with microflowers by a very simple, mild chemical precipitation method without templates or surfactants used. Furthermore, various pore sized cobalt pyrophosphate microflower materials have also been obtained by different thermal decompositions of the as-synthesized $\text{NH}_4\text{CoPO}_4\cdot\text{H}_2\text{O}$ microflowers in the air. The electrochemical properties of $\text{NH}_4\text{CoPO}_4\cdot\text{H}_2\text{O}$ microflowers and porous $\text{Co}_2\text{P}_2\text{O}_7$ materials are studied systematically for their using as electrochemical capacitor electrodes in different alkaline electrolytes. We found that among these materials, $\text{NH}_4\text{CoPO}_4\cdot\text{H}_2\text{O}$ microflowers exhibit larger supercapacitive characteristics in 1.0 M KOH electrolyte than others. The specific capacitance of $\text{NH}_4\text{CoPO}_4\cdot\text{H}_2\text{O}$ microflowers electrodes are up to 525 F g^{-1} at a current density of 0.625 A g^{-1} and have a long cycle life which have maintained 99.4 % after 400 cycles in 1.0 M KOH.

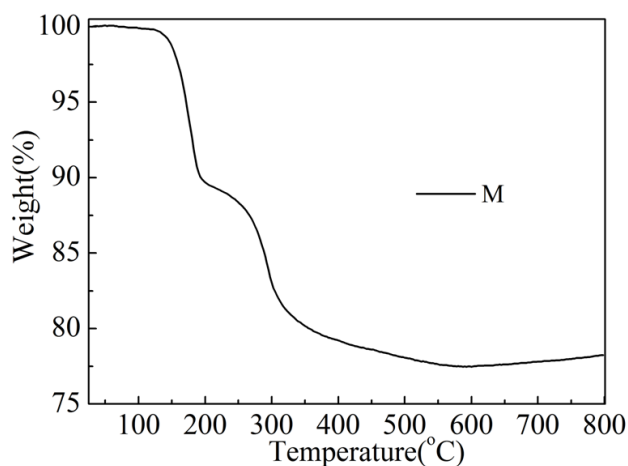
ACKNOWLEDGEMENTS

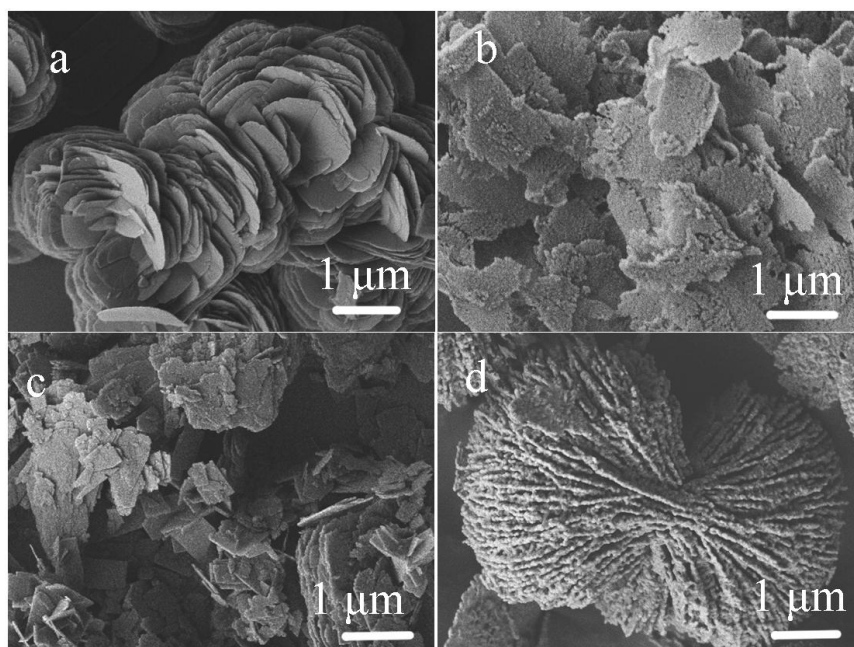
This work is supported by the National Natural Science Foundation of China (21201010, 21073129, 21071006), the Department of Science and technology of China for the 863 project (2009AA03Z225863). Henan Province of Science & Technology Foundation (122102210253) and the project of Science & Technology of Anyang city.

References

1. T. J. Barton, L. M. Bull, W. G. Klemperer, D. A. Loy, B. McEnaney, M. Misono, P. A. Monson, G. Pez, G. W. Scherer, J. C. Vartuli and O. M. Yaghi, *Chem. Mater.* 11 (1999) 2633.
2. J. N. Cha, G. D. Stucky, D. E. Morse and T. J. Deming, *Nature* 403 (2000) 289.
3. N. C. Seeman, *Nature* 421 (2003) 427.
4. K. Tanaka, G. H. Clever, Y. Takezawa, Y. Yamada, C. Kaul, M. Shionoya and T. Carell, *Nat. Nanotechnol.* 1 (2006) 190.
5. H. Ohgi, T. Maeda, E. Hosono, S. Fujihara and H. Imai, *Cryst. Growth Des.* 5 (2005) 1079.
6. G. H. Jeong, M. J. Kim, Y. W. Lee, W. J. Choi, W. T. Oh, Q. H. Park and S. W. Han, *J. Am. Chem. Soc.* 131 (2009) 1672–1673.
7. B. T. Holland, C. F. Blanford and A. Stein, *Science* 281 (1998) 538.
8. H. Cao, Y. Xu, J. Hong, H. Liu, G. Yin, B. Li, C. Tie and Z. Xu, *Adv. Mater.* 13 (2001) 1393.
9. T. Martensson, P. Carlberg, M. Borgström, L. Montelius, W. Seifert and L. Samuelson, *Nano Lett.* 4 (2004) 699.
10. R. Ma, Y. Bando, L. Zhang and T. Sasaki, *Adv. Mater.* 16 (2004) 918.
11. X. Wang and Y. Li, *Chem. Eur. J.* 9 (2003) 300.
12. Y. Zhao, Y. Xie, S. Yan and X. Zhu, *Chem. Mater.* 20 (2008) 3959–3964.
13. X. F. Shen, Y. S. Ding, J. Liu, J. Cai, K. Laubernds, R. P. Zerger, A. Vasiliev, M. Aindow and S. L. Suib, *Adv. Mater.* 17 (2005) 805.
14. K. H. An, W. S. Kim, Y. S. Park, Y. C. Choi, S. M. Lee, D. C. Chung, D. J. Bae, S. C. Lim and Y. H. Lee, *Adv. Mater.* 13 (2001) 497.
15. G. Arabale, D. Wagh, M. Kulkarni, I. S. Mulla, S. P. Vernekar, K. Vijayamohanan and A. M. Rao, *Chem. Phys. Lett.* 376 (2003) 20.
16. T. N. Ramesh, P. V. Kamath and C. Shivakumava, *J. Electrochem. Soc.* 152 (2005) 871.
17. Z. Fan, J. H. Chen, K. Z. Cui, F. Sun, Y. Xu and Y. F. Kuang, *Electrochim. Acta.* 52 (2007) 2959–2965.
18. J. K. Chang, M. T. Lee, C. H. Huang and W. T. Tsai, *Mater. Chem. Phys.* 108 (2008) 124–131.
19. C. C. Hu and W. C. Chen, *Electrochim. Acta.* 49 (2004) 3469.
20. H. K. Xin, W. Q. Fu, Z. X. Gang and W. X. Lei, *J. Electrochem. Soc.* 153 (2006) 1568.
21. G. Q. Zhang, Y. Q. Zhao, F. Tao and H. L. Li, *J. Power Sources.* 161 (2006) 723–729.
22. F. Tao, Y. Q. Zhao, G. Q. Zhang and H. L. Li, *Electrochem. Commun.* 9 (2007) 1282–1287.
23. C. Chen, W. Chen, J. Lu, D. Chu, Z. Huo, Q. Peng and Y. Li, *Angew. Chem., Int. Ed.* 48 (2009) 4816.
24. C. Morgovan, E. Marian, A. Iovi, I. Bratu and G. Borodi, *Rev. Chim.* 60 (2009) 1282.
25. H. Jiang, T. Zhao, C. Li and J. Ma, *J. Mater. Chem.* 21 (2011) 3818.
26. I. S. Cho, D. W. Kim, S. Lee, C. H. Kwak, S. T. Bae, J. H. Noh, S. H. Yoon, H. S. Jung, D. W. Kim and K. S. Hong, *Adv. Funct. Mater.* 18 (2008) 2154.
27. S. G. Carling, P. Day and D. Visser, *Inorg. Chem.* 34 (1995) 3917.
28. A. Q. Yuan, J. Wu, L. J. Bai, S. M. Ma, Z. Y. Huang and Z. F. Tong, *J. Chem. Eng. Data.* 53 (2008) 1066.
29. C. F. Zeng, W. W. Ji and L. X. Zhang, *CrystEngComm* 14 (2012) 3008–3011.
30. Y. M. Leeuwen, K. P. Velikov and W. K. Kegel, *RSC Adv.* 2 (2012) 2534–2540.
31. S. Okada, S. Sawa, M. Egashira, J. Yamaki, M. Tabuchi, H. Kageyama, T. Konishi and A.

- Yoshino, *J. Power Sources* 97–98 (2001) 430.
32. A. Yamada, M. Hosoya, S. C. Chung, Y. Kudo, K. Hinokuma, K. Y. Liu and Y. Nishi, *J. Power Sources* 119–121 (2003) 232.
33. C. Y. Nan, J. Lu, C. Chen, Q. Peng and Y. D. Li, *J. Mater. Chem.* 21 (2011) 9994.
34. X. Wang, J. Zhuang, Q. Peng and Y. D. Li, *Nature* 437 (2005) 121.
35. H. Pang, Z. Z. Yan, W. Wang, Y. Wei, X. Li, J. Li, J. Chen, J. S. Zhang and H. H. Zheng, *Int. J. Electrochem. Sci.*, 7 (2012) 12340-12353
36. H. Pang, J. W. Deng, B. Yan, Y. Ma, G. Li, Y. Ai, J. Chen, J. Zhang, H. Zheng and J. Du, *Int. J. Electrochem. Sci.*, 7 (2012) 10735-10747.
37. P. Feng, X. Bu and G. D. Stucky, *J. Solid State Chem.* 131 (1997) 160.
38. H. Pang, Y. Y. Liu, J. Li, Y. H. Ma, G. C. Li, Y. N. Ai, J. Chen, J. S. Zhang and H. H. Zheng, *Nanoscale*, 2013, 5, 503.
39. S. Okada, S. Sawa, M. Egashira, J. Yamaki, M. Tabuchi, H. Kageyama, T. Konishi and A. Yoshino, *J. Power Sources* 97–98 (2001) 430.
40. A. Yamada, M. Hosoya, S. C. Chung, Y. Kudo, K. Hinokuma, K. Y. Liu and Y. Nishi, *J. Power Sources* 119–121 (2003) 232.
41. H. Pang, Z. Z. Yan, W. Q. Wang, J. Chen, J. S. Zhang, H. H. Zheng, *Nanoscale*, 4 (2012) 5946.
42. H. Pang, B. Zhang, J. Du, J. Chen, J. Zhang and S. Li, *RSC Adv.* 2 (2012) 2257.
43. H. Pang, F. Gao, Q. Chen, R. Liu and Q. Lu, *Dalton Trans.* 41 (2012) 5862-5868
44. H. Pang, J. Deng, J. Du, S. Li, J. Li, Y. Ma, J. Zhang and J. Chen, *Dalton Trans.* 41 (2012) 10175–10181.
45. H. Pang, J. Deng, S. Wang, S. Li, J. Du, J. Chen and J. Zhang, *RSC Adv.* 2 (2012) 5930.
46. H. Pang, Y. F. Shi, J. M. Du, Y. H. Ma, G. C. Li, J. Chen, J. S. Zhang, H. H. Zheng and B. Q. Yuan, *Electrochim. Acta*, 85 (2012) 256–262.
47. L. H. Bao, J. F. Zang and X. D. Li, *Nano Lett.* 10 (2010) 1021.
48. K. Fic, G. Lota, M. Meller and E. Frackowiak, *Energy Environ. Sci.* 5 (2012) 5842-5850
49. S. L. Xiong, C. Z. Yuan, X. G. Zhang, B. J. Xi and Y. T. Qian, *Chem.–Eur. J.* 15 (2009) 5320.
50. J. C. Park, J. Kim, H. Kwon, H. Song, *Adv. Mater.* 21 (2009) 803–807.
51. C. C. Hu, K. H. Chang, M. C. Lin, Y. T. Wu, *Nano Lett.* 6 (2006) 2690–2695.
52. X. Xia, J. Tu, X. Wang, C. Gu, X. Zhao, *J. Mater. Chem.* 21 (2011) 671–679.
53. C. Z. Yuan, L. Chen, B. Gao, L. H. Su, X. G. Zhang, *J. Mater. Chem.* 19 (2009) 246–252.

ESI Fig. 1 TG patterns of $\text{NH}_4\text{CoPO}_4 \cdot \text{H}_2\text{O}$ microflowers



ESI Fig. 2 SEM images after 400 cycles in 1.0 M KOH solution (a) M; (b) P1; (c) P2; (d) P3.

ESI Table 1 the charge-transfer resistance R_{ct} of M, P1-P3.

	LiOH/ Ω	NaOH/ Ω	KOH/ Ω
M	10.1	5.5	4.1
P1	14.6	10.1	11.2
P2	29.8	22.5	36.7
P3	8.6	7.6	6.9